

Simulation of imaging and stray light effects in immersion lithography

Scott Hafeman* and Andrew R. Neureuther

Electronics Research Labs

Department of Electrical Engineering and Computer Sciences

University of California at Berkeley, Berkeley, CA 94720

ABSTRACT

Immersion lithography is a viable method for continuing the reduction in critical dimension. Much of the improvement in image quality in immersion lithography centers around high-NA vector imaging effects and in particular the roles of the resist coupling and polarization properties. Electromagnetic scattering from local inhomogeneities is considered yet emphasis is placed on the importance of accounting for high-NA, vector, immersion and resist standing wave effects. A new vector TCC formulation is introduced in SPLAT 6.0. The formulation is tested against a new theoretical formula for the Strehl ratio in air at high-NA and imaging 2D contact patterns at high NA in the resist stack.

Keywords: Immersion, Aerial Image, Vector Imaging, Transmission Cross-Coefficient, Polarization

1. INTRODUCTION

Immersion lithography is potentially impacted by a multitude of effects on many technical fronts. B.J. Lin gave an excellent overview of the many factors that potentially impact immersion lithography in a very early paper [1]. Immersion brings benefits such as an option to improve the working resolution, increase the depth of focus or both. Techniques for immersion lithography to extend the 193 nm node may also be applied to 157nm using a suitable type of liquid [2] to bring continued improvement in linewidth reduction [3].

The groundwork for characterizing effects of liquids in optical projection printing is being actively pursued by several other groups [2,4-8]. Some of the effects include interaction between the liquid and resist, propagation and scattering in inhomogeneous media, high-NA and polarization effects. A number of these effects are also dynamic and can even occur on a time-scale within a laser pulse. For example, a projection exposure may produce local pattern dependent heating of the resist that conductively heats the liquid that makes the liquid optically inhomogeneous introducing additional lateral scattering. It is important to account for these effects when simulating next generation optical lithography tools.

Much of the improvement in image quality in immersion lithography centers around high-NA vector imaging effects and in particular the roles of the resist coupling and polarization. T. Brunner pointed out the extraordinarily large enhancement of the poor contrast of the TM polarization with the effective high-NA in the resist seen with immersion [4]. Smith and Cashmore emphasized the disparity between TE and TM imaging [9]. Various models for high numerical aperture imaging have been proposed. Flagello et. al. first proposed a model for 3D numerical aperture imaging applied to optical lithography [10-11] and clearly demonstrated the difference in the TE and TM exposure of resist materials. Yeung et. al [12] provide a general vector Hopkins formulation of high-NA effects. They concluded that a single term average of the TE and TM effects was suitable up to NA of 0.7 and that resist coupling effects could be viewed as an additional aberration term in the pupil. Kirchaer [13] also provides equations for a TE/TM decomposition and off-axis rays. Collins [14] deals with an equivalent TCC interaction in three dimensions however it is not clear at this point on how the Zernike polynomial coefficients of much concern in optical lithography would be considered in his model.

The original intent of this paper was to use simulation of both electromagnetic scattering from local inhomogeneities and high-NA vector imaging to help identify effects in immersion lithography that potentially limit image quality. Section 2

* Correspondence: Phone (510) 642-8897, Fax (510) 642-2739, Email: shafeman@eecs.berkeley.edu

briefly surveys the potential for electromagnetic scattering from local inhomogeneities and explains our decision to focus our efforts instead on imaging effects. We quickly move on to a new and fully rigorous reformulation of high-NA vector imaging that is suitable for rapid image computation. Section 3 gives an overview of the generalization of Hopkins' method of image calculation based on high-NA vector-transmission cross coefficients and the detailed derivation is provided in Appendix A. Instead of using a general matrix of nine TCC terms in Eq 21 in Yeung, we simplify and consider only six coefficients, i.e. discard the contribution from the z-component as redundant at the entrance pupil plane. Several interesting properties of the cross terms and their size versus NA are given in Section 4 as well as Appendix B. The transformation conditions under which existing simulators can be utilized to emulate immersion lithography systems are given in Section 5. The initial implementation of the new high-NA vector formulation in the SPLAT aerial image simulator as version 6.0 is discussed in Section 6. Testing of the new simulator is considered in Section 7 and includes a new theoretical formula for the Strehl ratio in air at high-NA. Imaging of lines and most importantly the 2D patterns of contacts are considered in Section 8.

2. SCATTERING FROM LOCAL INHOMOGENITIES

The initial results for immersion lithography resist images reported by Switkes et. al [2] showed considerable line-edge roughness compared to resist images exposed in air. This led the authors to speculate on the possibility of various sources of optical noise in the exposure system. Possible scenarios included ghost images from multiple reflections back and forth across the liquid, speckle due to scattering from the prism surfaces, scattering from bubbles and turbulence and even local heating of the liquid or resist surface during the exposure process.

The likelihood of these various scenarios were tested or critiqued several ways. M. Switkes provided us a SEM GIF file which we analyzed by Fourier spectral methods. No evidence of a ghost reflection was observed. Further the spectral content did not show any evidence of wave contributions from speckle of off-axis waves. The possibility of scattering from local heating does not appear to be high. This is due to the fact that the heat rise per pulse is at most a few degrees and dn/dT is small and the fact that thermal diffusion distance in the time between pulses is much larger than a feature. Micron sized bubbles were not viewed as a likely source as the liquid surface tension would make their internal pressure exceed the vapor pressure and the gas would be reabsorbed quickly.

From the above considerations we concluded that the line-edge roughness resulted from the interaction of the immersion liquid with the resist rather than an electromagnetic effect. Meanwhile from the literature and discussions at workshops it became increasingly clear to us that the primary problem in achieving good image quality in immersion or any high-NA system is the loss of co-linearity in the TM or radial polarization. We thus focused our energy in developing immersion 2-D image simulator including a polarized for eliminating the low contrast radial electric field. Since this simulator includes lens aberrations its development will also allow us at a later date to investigate any macro inhomogeneities in the immersion liquid that might be shown exist.

3. VECTOR IMAGING MODEL

Our model is based on generalizing the scalar TCCs as first noted by Hopkins [15]. These TCCs describe the interaction of light traveling through different paths in the optical system before interfering on the imaging plane. The degree of interference is based on the partial coherence sigma of the source. The proposed model builds on the thin film formulation by Yeung [12] already in SPLAT as a vector extension to TCCs and follows a similar development as Adam [16]. The vector algebra up to the wafer plane results in the same expressions as Flagello [11] when considering the direction of the plane wave strictly dictated by its spatial harmonic thus having a predetermined location where the wave hits the entrance pupil in our model. Our algebraic model assumes that E_x and E_y are known on a mathematical plane just below the mask. These two field components are sufficient to calculate the both the magnitudes and phases of a set of plane waves in space that are equivalent anywhere below the mask to the effect of the mask itself. For simplicity we assume that these scattered field components do not change with angle of incidence other than a linear phase factor. However, this could be generalized to cover the full vector effects at entrance pupil if necessary by considering various zones of illumination over which the source components are invariant.

We compose our model by tracing one plane wave from the source plane to the image plane in the resist. An overview of the formulation will be provided here while the detailed mathematical derivations are provided in Appendix A. Figure 1 describes the optical system for projection printing. The column on the left denotes the reference planes in the imaging system along with the subscripts used to denote variables pertaining to that plane. The column along the right lists factors influencing aerial image formation residing at each reference plane. The basic behavior of the optical projection printing system is as follows. Light is emitted from the source and travels in a near-normal incident path to the mask. The light passes through portions of the mask producing a particular near field intensity. The near field can be expanded as a series of plane waves mutual orthogonal in the spatial frequency domain. These plane waves are captured at the entrance pupil where the image is reduced by the projection optics. Assuming a diffraction-limited system, some of these plane waves cannot propagate out towards the wafer plane. The final aerial image can be calculated at any depth in the resist using thin film techniques and projecting the E-field into Cartesian coordinates.

We now examine the path of one ray from the source plane to the resist image plane through other planes in the optical lithographic system. Without loss of generality, consider the path a wave takes whose E-field is oriented in the x-direction. After the wave scatters from the mask, the electric field hits the entrance pupil and can be split into radial and tangential components. The tangential component propagates to the exit pupil without a change in orientation however the radial component is tilted partially in the z-direction. The wave reaches the wafer where it is partially transmitted into the photoresist depending on the standing wave coefficient from the surface to the image plane. The ray changes angle according to Snell's law before reaching the image plane. Accounting for subscripts as listed in Figure 1 the representation of the E-field at the image plane is given as:

$$E_{xR} = E_{rp} t_{\parallel} S_{TM}(\theta_w) \cos \theta_R \cos \phi_p - E_{\phi p} t_{\perp} S_{TE}(\theta_w) \sin \phi_p \quad (3.1)$$

$$E_{yR} = E_{rp} t_{\parallel} S_{TM}(\theta_w) \cos \theta_R \sin \phi_p + E_{\phi p} t_{\perp} S_{TE}(\theta_w) \cos \phi_p \quad (3.2)$$

$$E_{zR} = -E_{rp} t_{\parallel} S_{TM}(\theta_w) \sin \theta_R \quad (3.3)$$

$$\text{where } \cos \phi_p = \frac{(f + f^{\#})}{\sqrt{(f + f^{\#})^2 + (g + g^{\#})^2}} \quad \sin \phi_p = \frac{(g + g^{\#})}{\sqrt{(f + f^{\#})^2 + (g + g^{\#})^2}} \quad (3.4-5)$$

$$\cos \theta_R = \sqrt{1 - \left(\frac{n_{med}}{n_{res}} k_{xy} \right)^2} \quad \sin \theta_R = \left(\frac{n_{med}}{n_{res}} k_{xy} \right) \quad \theta_w = \cos^{-1} \left(\sqrt{1 - k_{xy}^2} \right) \quad (3.6-8)$$

The coordinates $(f^{\#}, g^{\#})$ correspond to the pupil position for either the first or second pupil while (f, g) represents the point of integration as shown in Figure 2. The obliquity factor, scattering coefficient, and aberrations depend on the mask and pupil positions and act equally on all Cartesian components.

In order to utilize Hopkins method, the TCC must be generalized to the interaction of vector waves oriented at different angles when passing through the lens. Since the E-field at the image plane is now a vector quantity, the degree of mutual interference corresponds to a complex dot-product operation. Therefore, a vector formulation for the transmission cross coefficient is given by:

$$\text{TCC}(\hat{f}', \hat{g}'; \hat{f}'', \hat{g}'') = \int_{\Omega} \int \tilde{J}(\hat{f}', \hat{g}') (E_{f', g'} \bullet E_{f'', g''}^*) \tilde{P}(\hat{f} + \hat{f}', \hat{g} + \hat{g}') \tilde{P}^*(\hat{f} + \hat{f}'', \hat{g} + \hat{g}'') d\hat{f} d\hat{g} \quad (3.9)$$

Figure 2 depicts the region where numerical integration of the transmission cross-coefficient. \tilde{J} represents the mutual coherence circle of radius σ , \tilde{P} is the aberration due affecting the first plane wave \tilde{P}^* is the aberration affecting the second plane wave. The region Ω corresponds to the intersection of three circles: two shifted pupil circles of unit radius centered at (f', g') and (f'', g'') as well as a circle in standard position with radius σ .

4. VECTOR INTERACTION PROPERTIES

Consider the properties of the vector dot product term added to the transmission cross coefficient. For simplicity of the formulation, consider an ideal immersion lens where the full benefit of the refractive index can be utilized. Such a situation arises when the rays enter the immersion medium at normal incidence [17]. In this case, $t_{\parallel} = t_{\perp}$ for every pair of waves. To simplify the notation, denote $E_{f',g'}$ and $E_{f'',g''}$ as E_i and E_j respectively and hide the angular dependence of the TE and TM standing wave coefficients in the thin film stack for $q=i,j$ so that:

$$S_{TM}(\theta_{wq}) = S_{TMq} \quad S_{TE}(\theta_{wq}) = S_{TEq} \quad (4.1)$$

The dot product can be grouped into high NA and low NA terms:

$$D(i, j) = (E_i \cdot E_j) = E_{i,j \text{ lowNA}}(\theta_{Ri}, \theta_{Rj}, \phi_{pi} - \phi_{pj}) + E_{i,j \text{ highNA}}(\theta_{Ri}, \theta_{Rj}, \phi_{pi} - \phi_{pj}) \quad (4.2)$$

where:

$$\begin{aligned} D_{\text{lowNA}}(\theta_{Ri}, \theta_{Rj}, \phi_{pi} - \phi_{pj}) = & E_{rpi} E_{rpi} [S_{TMi} S_{TMj}] [\cos \theta_{Ri} \cos \theta_{Rj} \cos(\phi_{pi} - \phi_{pj})] \\ & + E_{rpi} E_{\phi pj} [S_{TMi} S_{TEj}] [\cos \theta_{Ri} \sin(\phi_{pi} - \phi_{pj})] \\ & - E_{\phi pi} E_{rpi} [S_{TEi} S_{TMj}] [\cos \theta_{Rj} \sin(\phi_{pi} - \phi_{pj})] \end{aligned} \quad (4.3)$$

and

$$\begin{aligned} D_{\text{highNA}}(\theta_{Ri}, \theta_{Rj}, \phi_{pi} - \phi_{pj}) = & E_{rpi} E_{rpi} [S_{TMi} S_{TMj}] [\sin \theta_{Ri} \sin \theta_{Rj}] \\ & + E_{\phi pi} E_{\phi pj} [S_{TEi} S_{TEj}] \cos(\phi_{pi} - \phi_{pj}) \end{aligned} \quad (4.4)$$

The first term listed in the low NA grouping shows the interaction of the TM components whose magnitude in the x-y plane is proportional to the cosine of the zenith angle for both rays. Additional terms are present at low NA that account for differences between standing waves formed from TE versus TM waves.

The first term in the high NA equation accounts for the negative interaction of the z components in rays originating from opposite sides of the lens. The second term accounts for the alignment of the TE components oriented on the x-y plane. The second term is the desired component in high NA imaging.

One interesting property is the interaction at the image plane of source fields oriented in the x-direction with fields oriented in the y-direction. In the simplest case when $i=j$, the algebra reduces to:

$$D(i_x, i_y) = (1/2) E_{xi} E_{yi} \sin(2\phi_{pi}) [S_{TMi}^2] (1 - \cos^2(\theta_i - \theta_i)) \quad (4.5)$$

The final multiplying factor accounts for the difference between the TE and TM transmission coefficients assuming a semi-infinite medium. Figure 3 displays the effect of this cross term when used in a dry system versus in an immersion system relative to the other coefficients in the dot product, i.e. only $(1 - \cos^2(\theta_i - \theta_i))$ is compared. We assumed a refractive index of 1.72 for the photoresist and a refractive index of water of 1.437 at 193 nm [9].

In the dry imaging systems, this term has a magnitude of approximately 5% relative to the self-interaction terms in a system with a NA of 0.65 when high NA imaging effects start to appear. At Brewster's angle in the dry system, this cross-term exceeds 10% of the relative magnitude of self-interaction terms as NA approaches 0.85. In comparison, the immersion system reaches 5% cross-term interaction only as NA increases beyond NA of 0.92, well beyond the Brewster Angle for the water-resist interface corresponding to NA of 0.762.

Appendix B illustrates additional basic properties of the dot product such as algebraic substitution of x and y oriented E-fields, verifying that a self-interaction of unity occurs in the on-axis case and that rotational symmetry exists in the x-y plane.

5. IMMERSING EXISTING SIMULATORS

This section outlines a set of four substitutions that allows any aerial simulator correctly account for the effects of introducing an immersion liquid between the exit pupil and the wafer plane. Several assumptions before making made when proposing these changes and they should not be applied blindly without understanding their implications to the particular simulation program in use. The modifications assume that the refractive index of the immersion liquid is relatively low ($n < 2$) so that when the demagnification factor is scaled the rays at the edge of the entrance pupil still have a negligible component in the z-direction. Otherwise, a more rigorous model will be needed to model the 3D orientation of the x-oriented and y-oriented E-fields at the entrance pupil. Lastly, it is important to understand the implications of these changes in other parts of the program as the following formulation is based on the manipulation of internal variables in SPLAT 5.0.

Introducing an immersion liquid alters the imaging wavelength, the zenith angle of incidence on the wafer and also alters the E-field coupling into the resist thin film stack. Assume that NA_a is the effective numerical aperture in air that the user provided for the aerial image simulator. The first obvious substitution is reducing the wavelength by n_{med} . In order to correct for the numerical aperture, using Snell's law and the definition of numerical aperture:

$$\frac{\sin \theta_t}{\sin \theta_i} = \frac{NA_t}{NA_i} = \frac{n_i}{n_t} \quad \therefore \hat{NA} = \frac{NA}{n_{med}} \quad (5.1)$$

To maintain the E-field coupling into the resist thin film stack, consider Snell's law and other related functions:

$$\sin \theta_t = \frac{n_i}{n_t} \sin \theta_i \quad \therefore \{\sin \theta_t, \cos \theta_t, \cos \theta_i\} \in f\left(\sin \theta_i, \frac{n_i}{n_t}\right) \quad (5.2)$$

The reflection and transmission coefficients for parallel and sagittal orientations can be expressed as functions of elementary sine and cosine relations of the incident and transmitted zenith angles. Therefore, the third scaling rule is to reduce the indices of refraction of all materials in the optical path by a factor of n_{med} . The fourth scaling factor refers to the entrance pupil acceptance cone. If NA represents the effective numerical aperture in air, the numerical aperture at the entrance pupil is NA/M_{demag} where M_{demag} denotes the optical demagnification factor. In order to maintain the numerical aperture at the entrance pupil when scaling NA to \hat{NA} then the optical demagnification factor must be reduced by a factor of n_{med} . This adjusts the obliquity factor in an appropriate manner.

As an example, consider Figure 4 depicting the entrance and exit pupils of a 4x demagnification system with $NA_o=0.8$ at the exit pupil for a dry imaging system and an ideal wet imaging system immersed with a liquid of $n=1.5$ to achieve an effective NA_o of 1.2 in air. Assuming that the optical system is diffraction limited at the exit pupil, the physical ray cone dictating the numerical aperture is always constrained to 0.8. However, the zenith angle from the lens to the immersion liquid at the exit pupil can be larger since there is less constraint on the critical angle leading to total internal reflection. In effect, this allows a larger numerical aperture of rays at the entrance pupil to be transferred through the exit pupil. The increase is proportional to the refractive index of the immersion liquid. Therefore the demagnification factor should be decreased by a factor of n_{med} for the purposes of calculating the obliquity factor and normalization constant as detailed in Cole et. al. [18]. Image reconstruction in the immersion liquid requires that spatial frequencies be scaled by n_{med} equivalent to a reduction in wavelength. In summary, the following transformations can be used in order to simulate immersion lithography:

$$\hat{\lambda} = \frac{\lambda}{n_{med}} \quad \hat{NA} = \frac{NA}{n_{med}} \quad \hat{n}_{material} = \frac{n_{material}}{n_{med}} \quad \hat{M}_{demag} = \frac{M_{demag}}{n_{med}} \quad (5.3)$$

6. IMPLEMENTATION

Using Hopkins theory of partially coherently imaging, the total image is the integration of the transmission cross-coefficients over all available pairs of object spectra $O(f,g)$ where the scalar TCC has been replaced with Eq (3.9) as described in Section 4 and derived in Appendix A:

$$I = \iiint_{f'',g''} \iiint_{f',g'} TCC(\hat{f}', \hat{g}'; \hat{f}'', \hat{g}'') \tilde{O}(\hat{f}', \hat{g}') \tilde{O}^*(\hat{f}'', \hat{g}'') \\ \cdot \exp(-i2\pi[(\hat{f}' - \hat{f}'')x + (\hat{g}' - \hat{g}'')y]) d\hat{f}' d\hat{g}' d\hat{f}'' d\hat{g}'' \quad (6.1)$$

Equation (6.1) is the basis for SPLAT version 6.0, which accounts for the vector nature of the interaction of light. The current version of this code has been implemented in Fortran within the existing program architecture of Splat 5.0. The program is currently in a non-optimal state and Ongoing verification of this image model is in progress by comparing SPLAT 6.0 to existing results in works such as [4],[7],[9], [19]. Algorithms for the detection of symmetry were bypassed to ensure correctness leading to an increase of up to 16 times as many TCC calculations involving numerical integration. In the case of calculating the image in air, no additional loops are required so only the symmetry penalty is incurred. In the case when the image plane is inside the resist, there has not been an appropriate look-up table for the vector case so there is an extreme penalty for resist-coupled cases at the moment. This will likely improve in the near future as functionality is added to SPLAT 6.0 and the symmetry detection algorithm is generalized for the vector TCC. In the optimal case, the incurred penalty could reach a factor of 2 or 3 over the scalar case at high NA even for image plane calculations inside the resist.

7. VERIFYING THE VECTOR MODEL

This section formulates and compares the calculated and simulated values for a small 2D feature in SPLAT 6.0. We position an isolated $0.2 \lambda/NA$ contact at the center of the mask. This feature is sub-printable and approximates a pinhole so we assume that the mask scatters light in all directions, filling the entrance pupil uniformly. In order to simplify the TCC integration, we tested our vector model with a partial coherence of 0.05. The transmission coefficient between the exit pupil and immersion liquid is identical for all pupil positions assuming an ideal immersion system and can be factored from the expressions in Eq (3.9). Therefore, the E-field in air when neglecting the effects of the resist is:

$$E_{xR} = E_p \cos \theta_R \cos \phi_p - E_\phi \sin \phi_p \quad (7.1)$$

$$E_{yR} = E_p \cos \theta_R \sin \phi_p + E_\phi \cos \phi_p \quad (7.2)$$

$$E_{zR} = -E_p \sin \theta_R \quad (7.3)$$

Supposing now that the E-field incident on the mask is oriented in the x-direction, we can substitute the radial and tangential fields. The E-fields can be integrated over the pupil plane from $0 < \phi_p < 2\pi$ and $0 < r < 1$. Integration of E_{yR} and E_{zR} over the pupil plane yield zero but over E_{xR} :

$$E_{xR} = E_p \left[\int_{\phi=0}^{2\pi} \int_{r=0}^1 \cos \theta_R \cos^2 \phi_p r dr d\theta - \int_{\phi=0}^{2\pi} \int_{r=0}^1 \sin^2 \phi_p r dr d\theta \right] \quad (7.4)$$

Noticing that the zenith angle is a function of r and is constrained from $0 < \theta_R < NA$. Using $\sin(\theta_R) = rNA$ and substituting $p = rNA$, integration yields:

$$E_{xR} = 2\pi E_{xp} \left[1 - \frac{1}{2} \left[1 - \frac{2(1 - (1 - NA^2)^{3/2})}{3NA^2} \right] \right] \quad (7.5)$$

This can be viewed as a perturbation of the scalar case as NA changes so that the normalized field is:

$$\bar{E}_{xR} = 1 - \Delta \quad \text{where} \quad \Delta = \frac{1 - (1 - NA^2)^{3/2}}{3NA^2} \quad (7.6)$$

A comparison of the scalar versus vector versions of Splat against equation (7.6) is shown in Figure 5. \bar{E}_{xR} in the scalar version 5.0 remains constant whereas the vector version 6.0 predicts the value to within the numerical error of the simulation program. Be aware that this case does not validate that the vector model is correct, it has just shown that reasonable assumptions and careful programming were used to verify a simple case. The derivation was carried out for a demagnification factor of one where there are non-negligible z-components. We are developing additional scenarios where analytical analysis results in a closed form solution that can be used to test our vector model.

8. SIMPLE PATTERNS

This section shows three simple cases where the new models in SPLAT 6.0 can be used. The first case shows: the difference between scalar and vector imaging at high NA. The second case compares image formation within the resist for a dry and immersion system with comparable parameters. The third case displays the effect of introducing a pupil plane filter and imaging solely with the TE or TM waves.

We chose to use a $0.55 \lambda/NA$ L=S PSM pattern to compare the use of scalar and vector imaging predictions at high NA. The optical system we used was 4x demagnification, $\sigma = 0.1$ and NA ranging from 0.7 to 0.9. Photoresist interaction was neglected for these simulations. Figure 6 and Figure 7 plot the intensity in air for the Splat 5.0 and Splat 6.0 respectively. Both simulators predict the frequency-doubling phenomenon however Splat 5.0 overestimates the peak intensity that should theoretically be 2.0. Splat 6.0 predicts that the quality of the nulls will eventually be degraded since there is no longer total vector cancellation at high angles of incidence.

For the second case of simple patterns we considered an isolated contact of size $0.7 \lambda/NA$ at $NA = 0.85$ and σ of 0.3. A homogeneous photoresist film 300nm thick with $n = 1.72$ is used choosing a substrate producing a 15% E-field reflection coefficient. The aerial image is calculated inside the resist at a depth of 50 nm. The aerial image in the resist using 157 nm in air is shown in Figure 8 while the same image in the resist using 193 nm in water immersion is shown in Figure 9. Both the scalar and vector models show a greater degree of coupling to the resist stack when using water immersion as a result of a higher transmission coefficient into the resist. The scalar model overestimates the image formed using the vector model in Figure 8. The vector model shows that the resist coupling at 193 nm as mitigated by immersion gives nearly a 4x improvement in the brightness of small 2D features.

Finally we observe the predicted effects of inserting a polarization filter at the pupil plane [20] to improve image quality at high NA. We use the same mask topology, imaging parameters and resist image plane as above except we use 193 nm in air. The intensity cut lines for the TE image and TM image at a 50 nm depth inside the resist are plotted in Figure 10. The TE and TM intensities can be directly compared to those shown in Figures 8 and 9. The image formed by filtering TM waves at the pupil plane has higher peak intensity and better image quality than its counterpart. The major disadvantage in implementing such a filter is that approximately 40% of the non-filtered intensity is imaged in the resist raising issues such as insufficient exposure, thermal absorption or reflection by a real filter.

9. CONCLUSIONS

We introduced a new high-NA vector transmission cross-coefficient. The formulation permitted us to separate the high-NA and low-NA terms, present qualitative insight and show that orthogonal source x and y e-fields lose their orthogonality more severely in dry systems compared to immersion systems. We also introduced and verified a new

theoretical formula for the Strehl ratio in air at high-NA using SPLAT 6.0. We considered imaging of 2D contact patterns in Section 8. The peak intensity for these small features in the resist improved fourfold with immersion primarily from improving the resist coupling.

10. ACKNOWLEDGEMENTS

The lithography research was supported by SRC under grant 2001-MC-460 and DARPA under grant DA972-01-1-0021. The authors would like to thank Michael Switkes for his discussions and insight into the effects observed in his SEM images. The authors would also like to thank Kostas Adam and Thomas Pistor for their suggestions in formulation of the vector extension to the TCC.

11. REFERENCES

1. B. J. Lin, "The Future of subhalf-micrometer optical lithography", *Microelectronic Engineering* vol. 6, p. 31-51, (1987)
2. M. Switkes, M. Rothschild, "Resolution Enhancement of 157 nm Lithography by Liquid Immersion", *Proc. SPIE* 4691, 450-465 (2002)
3. L. Van den hove, A. M. Goethals, K. Ronse, M. Van Bavel, G. Vandenbergh, "Lithography for sub-90nm applications", *IEEE International Electron Devices Meeting*, Sec 1, pp 3-8 (2002)
4. T. A Brunner, N. Seong, W. D. Hindsberg, J. A. Hoffnagle, F. A. Houle, M. I Sanchez, "High NA Lithography Imagery at Brewster's Angle", *Proc. SPIE* 4691, 1-10 (2002)
5. B. J. Lin, "New A/NA scaling equations for resolution and depth-of-focus", *Proc SPIE* 4000, 759-764 (2000)
6. A. C. Wei, G. F. Nellis, A. Y. Abdo, C. Chen, R. L. Engelstad, W. A. Beckman, E. G. Lovell, M. Switkes, M. Rothschild, "Preliminary microfluidic simulations for immersion lithography", *Proc SPIE* 5040 (2003) [in press]
7. S. Y. Yeon, M. Rothschild, M. Switkes, D. C. Cole, M. S. Yeung, E. Barouch, "Simulation study of process latitude for liquid immersion lithography", *Proc SPIE* 5040 (2003) [in press]
8. A. K. Raub, S. R. J. Brueck, "Deep Deep UV immersion interferometric lithography", *Proc SPIE* 5040 (2003) [in press]
9. B. W. Smith, J. Cashmore, "Challenges in High NA, Polarization and Resists", *Proc SPIE* 4691, 11-23 (2002)
10. D Flagello, "3D Modelling of High Numerical Aperture Imaging in Thin Films," *Proc. SPIE* 1625, 246-261 (1992)
11. D Flagello, T. Milster, A. E. Rosenbluth, "Theory of High NA imaging in Homogeneous Thin Films", *J. Opt. Soc. Amer. A*, Vol 13, No 1, 53-64 (1996)
12. M. S. Yeung, D. Lee, R. Lee, A. R. Neureuther, "Extension of the Hopkins theory of partially coherent imaging to include thin film interference effects", *Proc. SPIE* 1927, 452-463 (1993)
13. H. Kirchauer, "Photolithography Simulation", Ph. D Dissertation, Section 4.1.5, Institute for Microelectronics Memo E360/98, Technical University Vienna (1998)
14. M. R. Arnison, C. J. R. Sheppard, "A 3D vectorial optical transfer function suitable for arbitrary pupil functions", *Optics Communications*, 211, 53-63 (2002)
15. H. H. Hopkins, "On the Diffraction Theory of Optical Images", *Proc. Roy. Soc. A* 217, 408-432 (1953)
16. K. Adam, Y. Granik, N. B. Cobb, A. Torres, "Improved modeling performance with an adapted vectorial formulation of the Hopkins imaging equation and a variable threshold resist model", *Proc. SPIE* 5040 (2003) [in press]
17. B. W. Smith, H. Kang, A. Bourov, F. Cropanese, "Water immersion optical lithography for the 65- to 45-nm nodes", *Proc SPIE* 5040 (2003) [in press]
18. D. C. Cole, E. Barouch, U. Hollerbach, S.A. Orszag, "Derivation and Simulation of Higher Numerical Aperture Scalar Aerial Images", *Jap J. Appl. Phys., Part 1*, Vol 31, 4110-4119 (1992)
19. D. Flagello, "High Numerical Aperture Effects in Photoresist", *Applied Optics*, Vol. 36, No. 34, 8944-8951 (1997)
20. D. R. Sheats, B. Smith, *Microlithography: Science and Technology*, Marcel Dekker, pp 256 (1998)

APPENDIX A

This section provides the method used to derive the transfer of E-fields from the source plane to the image plane inside the resist. Figure 1 is used as a reference for defining the variables and subscripts for our vector model. Assume that each linearly polarized plane waves hit the mask whose polarizations are either in the x-direction or y-direction. Each of these waves has an electric field that can be split into a radial component with subscript r and a sagittal component with subscript Φ depending on where the wave hits the pupil:

$$\text{x-oriented:} \quad E_r = E_x \cos \phi_p \quad E_\phi = -E_x \sin \phi_p \quad (\text{A.1-2})$$

$$\text{y-oriented:} \quad E_r = E_y \sin \phi_p \quad E_\phi = E_y \cos \phi_p \quad (\text{A.3-4})$$

Analysis will proceed to the exit pupil where all rays transition between the exit lens and the medium above the wafer. Aberrations based on the OPD value on the pupil map affect all fields equally contributing to a temporal phase shift. When the rays enter the medium at the exit pupil, their amplitudes are modified by the parallel and perpendicular transmission coefficients. The lens designer would supply information about the entrance angle versus pupil position. To simplify the problem, assume that the rays enter the medium at nearly normal incidence for all pupil positions across the lens. This is the ideal immersion case where the imaging resolution increases by n_{med} . The transmission coefficient for either ray reduces to:

$$t_\perp = t_\parallel = \frac{2n_{lens}}{n_{lens} + n_{med}} \text{ so that } E_{rw} = E_r t_\parallel \text{ and } E_{\phi w} = E_\phi t_\perp \quad (\text{A.5-6})$$

where n_{lens} is the refractive index of the lens. This expression is constant for all rays and can be factored outside of the TCC integration. Combining these coefficients with the standing wave coefficients is possible depending on the type of prism used to couple light into the immersion liquid. The tangential field emerges from the exit pupil without any axial tilt however the radially oriented field is tilted at an angle θ_w with respect to the z-axis depending on its location on the exit pupil:

$$\cos \theta_w = \sqrt{1 - k_{xy}^2}, \quad k_x = \frac{f\lambda\pi}{L_x}, \quad k_y = \frac{g\lambda\pi}{L_y}, \quad k_{xy} = \sqrt{k_x^2 + k_y^2} \quad (\text{A.7-10})$$

Once the wave hits the resist, it goes through a multitude of reflections and transmissions modeled by upward and downward propagating plane waves derived by Yeung [12]. These coefficients are different for TE than for TM waves, corresponding to the tangential and radially oriented fields used in the derivation thus far. Denote these standing wave coefficients by $S_{TE}(\theta_w)$ and $S_{TM}(\theta_w)$ so that:

$$E_{rR} = S_{TM}(\theta_w) E_{rw} \quad \text{and} \quad E_{\phi R} = S_{TE}(\theta_w) E_{\phi w} \quad (\text{A.11-12})$$

The following angular relations hold based on the orientation of the problem space and Snell's law:

$$n_{med} \sin \theta_w = n_{res} \sin \theta_R \quad \phi_R = \phi_w = \phi_p \quad (\text{A.13-14})$$

Finally, the field is decomposed into its x, y and z coordinate orientations so that:

$$E_{xR} = E_{rR} \cos \theta_R \cos \phi_R - E_{\phi R} \sin \phi_R \quad (\text{A.15})$$

$$E_{yR} = E_{rR} \cos \theta_R \sin \phi_R + E_{\phi R} \cos \phi_R \quad (\text{A.16})$$

$$E_{zR} = -E_{rR} \sin \theta_R \quad (\text{A.17})$$

Substituting the results from Equations (A.5) through (A.14) into (A.15-17) yields:

$$E_{xR} = E_r t_\parallel S_{TM}(\theta_w) \cos \theta_R \cos \phi_p - E_\phi t_\perp S_{TE}(\theta_w) \sin \phi_p \quad (\text{A.18})$$

$$E_{yR} = E_r t_\parallel S_{TM}(\theta_w) \cos \theta_R \sin \phi_p + E_\phi t_\perp S_{TE}(\theta_w) \cos \phi_p \quad (\text{A.19})$$

$$E_{zR} = -E_r t_\parallel S_{TM}(\theta_w) \sin \theta_R \quad (\text{A.20})$$

$$\text{where } \cos \phi_p = \frac{(f + f^\#)}{\sqrt{(f + f^\#)^2 + (g + g^\#)^2}} \quad \sin \phi_p = \frac{(g + g^\#)}{\sqrt{(f + f^\#)^2 + (g + g^\#)^2}} \quad (\text{A.21-22})$$

$$\cos \theta_R = \sqrt{1 - \left(\frac{n_{med}}{n_{res}} k_{xy} \right)^2} \quad \sin \theta_R = \left(\frac{n_{med}}{n_{res}} k_{xy} \right) \quad \theta_w = \cos^{-1} \left(\sqrt{1 - k_{xy}^2} \right) \quad (\text{A.23-25})$$

The point $(f^\#, g^\#)$ used in the calculation of the azimuthal angles is the pupil position for either unit circle in Figure 2 centered at (f', g') or (f'', g'') .

APPENDIX B

This section elaborates on Appendix A by simplifying the dot product expression and considering some vector interaction properties under different circumstances. To simplify the notation, denote $E_{f',g'}$ and $E_{f'',g''}$ as E_i and E_j respectively. For two rays i and j , the dot product expression using Eqs. (A.18-20) becomes:

$$\begin{aligned} E_i \bullet E_j &= E_{xRi} E_{xRj} + E_{yRi} E_{yRj} + E_{zRi} E_{zRj} \\ &= [E_{rpi} t_{\parallel i} S_{TM}(\theta_{wi}) \cos \theta_{Ri} \cos \phi_{pi} - E_{\phi pi} t_{\perp i} S_{TE}(\theta_{wi}) \sin \phi_{pi}] \\ &\times [E_{rpj} t_{\parallel j} S_{TM}(\theta_{wj}) \cos \theta_{Rj} \cos \phi_{pj} - E_{\phi pj} t_{\perp j} S_{TE}(\theta_{wj}) \sin \phi_{pj}] \\ &+ [E_{rpi} t_{\parallel i} S_{TM}(\theta_{wi}) \cos \theta_{Ri} \sin \phi_{pi} + E_{\phi pi} t_{\perp i} S_{TE}(\theta_{wi}) \cos \phi_{pi}] \\ &\times [E_{rpj} t_{\parallel j} S_{TM}(\theta_{wj}) \cos \theta_{Rj} \sin \phi_{pj} + E_{\phi pj} t_{\perp j} S_{TE}(\theta_{wj}) \cos \phi_{pj}] \\ &+ [E_{rpi} t_{\parallel i} S_{TM}(\theta_{wi}) \sin \theta_{Ri}] \times [E_{rpj} t_{\parallel j} S_{TM}(\theta_{wj}) \sin \theta_{Rj}] \end{aligned} \quad (\text{B.1})$$

where \times is used for scalar multiplication. For simplicity, factor out the transmission coefficients and simplify the notation for $q = i$ or j by denoting:

$$S_{TM}(\theta_{wq}) = S_{TMq} \quad S_{TE}(\theta_{wq}) = S_{TEq} \quad t_{\parallel q} = t_{\perp q} = t = 1 \quad (\text{B.2-4})$$

Group terms in Eq (B.1) by field component products at the pupil plane reduces the dot product to:

$$\begin{aligned} (E_i \bullet E_j) &= \\ &E_{rpi} E_{rpj} [S_{TMi} S_{TMj}] [\cos \theta_{Ri} \cos \theta_{Rj} \cos(\phi_{pi} - \phi_{pj}) + \sin \theta_{Ri} \sin \theta_{Rj}] \\ &+ E_{rpi} E_{\phi pj} [S_{TMi} S_{TEj}] [\cos \theta_{Ri} \sin(\phi_{pi} - \phi_{pj})] \\ &- E_{\phi pi} E_{rpj} [S_{TEi} S_{TMj}] [\cos \theta_{Rj} \sin(\phi_{pi} - \phi_{pj})] \\ &+ E_{\phi pi} E_{\phi pj} [S_{TEi} S_{TEj}] \cos(\phi_{pi} - \phi_{pj}) \end{aligned} \quad (\text{B.5})$$

The dot product is a function of the difference between pupil angles as expected and exhibits rotational symmetry across the pupil. First, consider X wave or Y wave self-interaction. In the simple scenario when standing wave effects are neglected and assuming that i and j are equal then the dot product of two E-field vectors in air should yield the original field value squared. From (B.5):

$$E_i \bullet E_i = E_{rpi}^2 + E_{\phi pi}^2 (0 - 0) + E_{\phi pi}^2 = E_{rpi}^2 + E_{\phi pi}^2 \quad (\text{B.6})$$

For x-waves and for y-waves, use (B.5) to get:

$$E_{rpi}^2 + E_{\phi pi}^2 = E_x^2 \cos^2 \phi_{pi} + E_x^2 \sin^2 \phi_{pi} = E_x^2 \quad (\text{B.7})$$

$$E_{rpi}^2 + E_{\phi pi}^2 = E_y^2 \sin^2 \phi_{pi} + E_y^2 \cos^2 \phi_{pi} = E_y^2 \quad (\text{B.8})$$

Second, consider X and Y wave interaction when $i = j$. When wave i is transformed into an x-wave and wave j is transformed into a y-wave, the interaction when $i=j$ should be zero. Use (B.5), drop E product terms then substitute x and y waves from (A.1-2) to get:

$$(E_i \bullet E_j) = E_{xi} E_{yj} \cos \phi_{pi} \sin \phi_{pj} [S_{TM i} S_{TM j}] - E_{xi} E_{yj} \sin \phi_{pi} \cos \phi_{pj} [S_{TE i} S_{TE j}] \quad (B.9)$$

When $i=j$ then,

$$(E_i \bullet E_j) = \frac{1}{2} E_{xi} E_{yi} \sin(2\phi_{pi}) ([S_{TM i}^2] - [S_{TE i}^2]) \quad (B.10)$$

The conclusion is that x-waves and y-waves at the same point in the pupil plane don't show orthogonality at the wafer plane as NA increases. In order to gauge when these interactions are significant, consider a semi-infinite medium below the wafer plane. The ratio of the transmission coefficients for the two polarizations is:

$$\frac{\tau_{\perp}}{\tau_{\parallel}} = \left[\frac{2 \sin \theta_t \cos \theta_i}{\sin(\theta_i + \theta_t)} \right] / \left[\frac{2 \sin \theta_t \cos \theta_i}{\sin(\theta_i + \theta_t) \cos(\theta_i - \theta_t)} \right] = \cos(\theta_i - \theta_t) \quad (B.11)$$

so that,

$$[S_{TM i}^2] - [S_{TE i}^2] = [S_{TM i}^2] (1 - \cos^2(\theta_i - \theta_t)) \quad (B.12)$$

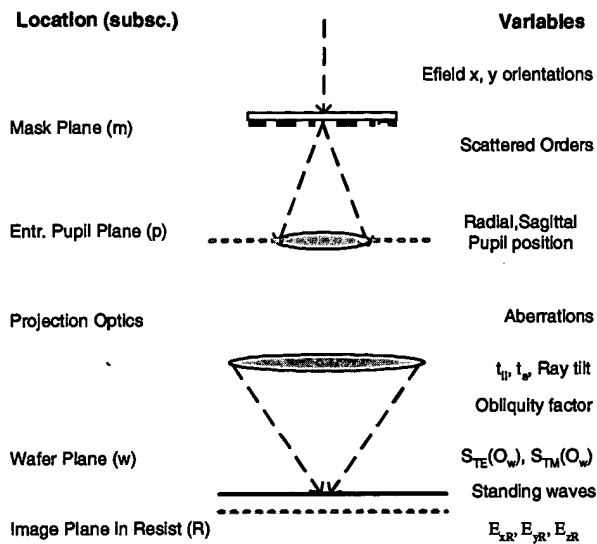


Figure 1 Optical Factors affecting a Projection Printing System

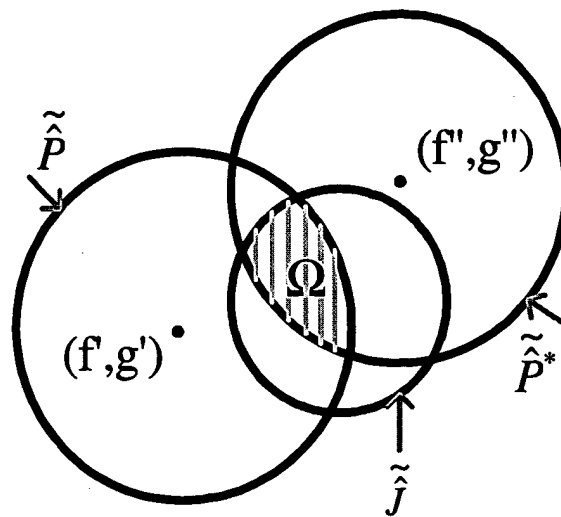


Figure 2 Region of Interaction Leading to the TCC

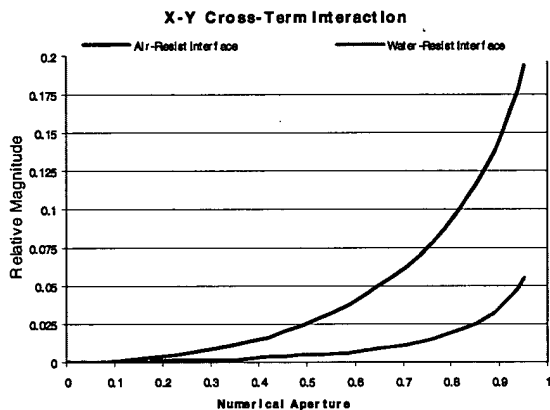


Figure 3 X-Y Cross Term Interaction versus NA for wet and dry systems

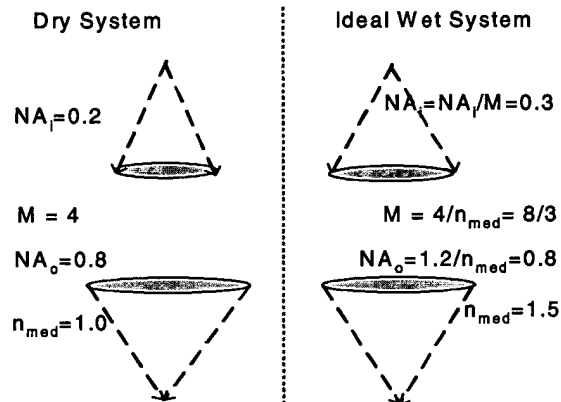


Figure 4 Change in Entrance and Exit Pupil Cones when adding an Immersion Liquid

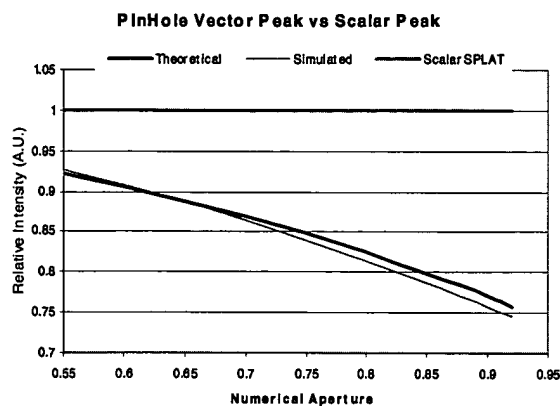


Figure 5 Comparison of Theoretical vs Computed Aerial Image formation of a $0.2 \lambda/\text{NA}$ pinhole in SPLAT 5.0 and SPLAT 6.0

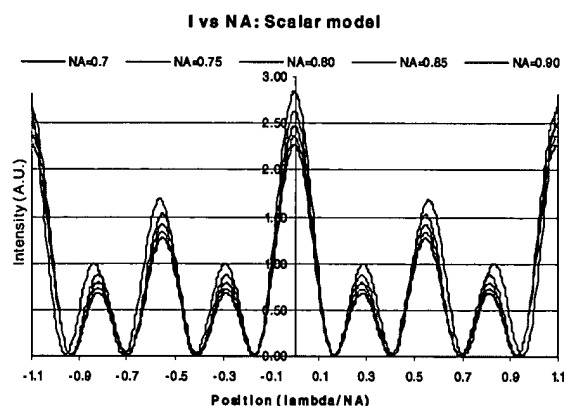


Figure 6 Aerial Image in Air, Scalar Model, $0.55 \lambda/\text{NA}$ L=S PSM with increasing NA

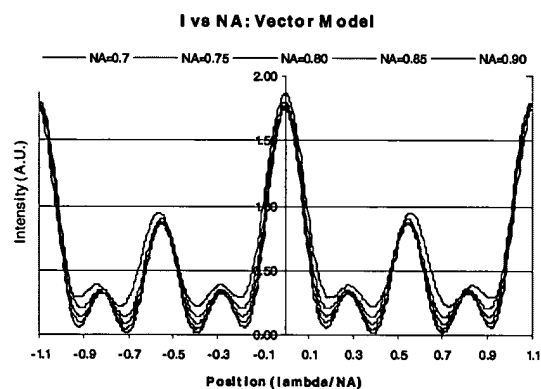


Figure 7 Aerial Image in Air, Vector Model, $0.55 \lambda/\text{NA}$ L=S PSM with increasing NA

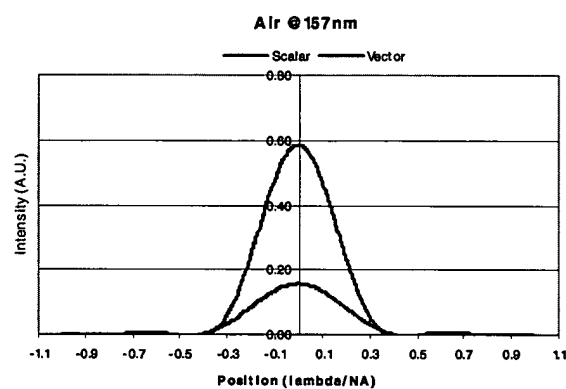


Figure 8 Air and 157 nm tool aerial imag in resist @ $z=50$ nm, $\text{NA}=0.85$, $0.7 \lambda/\text{NA}$ isolated contact

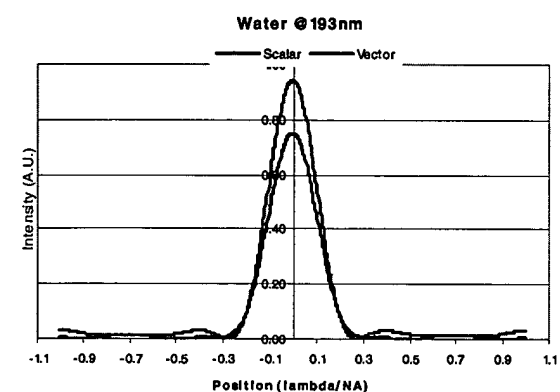


Figure 9 Water and 193 nm tool aerial Image using in resist @ $z=50$ nm, $\text{NA}=0.85$, $0.7 \lambda/\text{NA}$ isolated contact

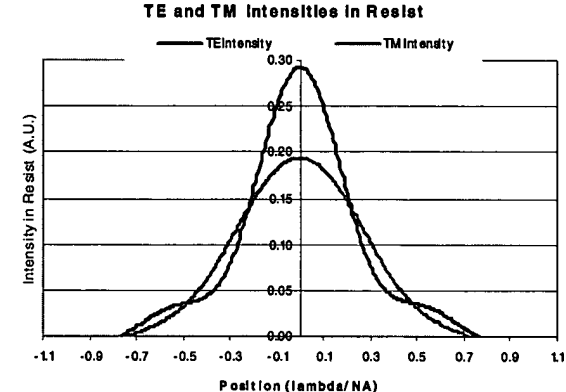


Figure 10 Aerial images through pupil plane filter, measured in resist @ $z=50$ nm, $\text{NA}=0.85$, $0.7 \lambda/\text{NA}$ isolated contact

